

Article

Coseismic Ground Deformation Reproduced through Numerical Modeling: A Parameter Sensitivity Analysis

Yuri Panara ^{1,*}, Giovanni Toscani ^{1,3}, Michele L. Cooke ² , Silvio Seno ^{1,3} and Cesare Perotti ^{1,3} 

¹ Department of Earth and Environmental Sciences, University of Pavia, Pavia I-27100, Italy

² Department of Geosciences, University of Massachusetts, Amherst, MA 01003, USA

³ CRUST (Centro inteRUniversitario per l'analisi SismoTettonica tridimensionale con applicazioni territoriali), Pavia I-27100, Italy

* Correspondence: yuri.panara01@universitadipavia.it

Received: 21 June 2019; Accepted: 22 August 2019; Published: 25 August 2019



Abstract: Coseismic ground displacements detected through remote sensing surveys are often used to invert the coseismic slip distribution on geologically reliable fault planes. We analyze a well-known case study (2009 L'Aquila earthquake) to investigate how three-dimensional (3D) slip configuration affects coseismic ground surface deformation. Different coseismic slip surface configurations reconstructed using aftershocks distribution and coseismic cracks, were tested using 3D boundary element method numerical models. The models include two with slip patches that reach the surface and three models of blind normal-slip surfaces with different configurations of slip along shallowly-dipping secondary faults. We test the sensitivity of surface deformation to variations in stress drop and rock stiffness. We compare numerical models' results with line of sight (LOS) surface deformation detected from differential SAR (*Synthetic Aperture Radar*) interferometry (DInSAR). The variations in fault configuration, rock stiffness and stress drop associated with the earthquake considerably impact the pattern of surface subsidence. In particular, the models with a coseismic slip patch that does not reach the surface have a better match to the line of sight coseismic surface deformation, as well as better match to the aftershock pattern, than models with rupture that reaches the surface. The coseismic slip along shallowly dipping secondary faults seems to provide a minor contribution toward surface deformation.

Keywords: coseismic ground deformation; active fault geometry; DInSAR; numerical models; sensitivity analysis

1. Introduction

Understanding the relationships between subsurface slip and coseismic ground deformation provides a foundation for many seismotectonic and seismic hazard assessment studies. Starting from the work of Massonnet in 1993 [1], remote sensing techniques have provided new important tools for the detection, observation and measurement of surface coseismic deformation (e.g., [2–5]). Differential SAR (*Synthetic Aperture Radar*) interferometry (DInSAR) analysis can measure coseismic surface deformation (e.g., [6]) and consequently, serve as input data for numerical models that invert for fault geometry and/or fault slip distribution (e.g., [2,3,5,7]). If fault geometry is well constrained, the inversions can produce reliable slip distributions that are consistent with seismic data [2,7]; for this reason, we used geologic and geophysical data in order to constrain a reliable fault configuration.

The L'Aquila seismic sequence (Figure 1) occurred in a seismically active region of central Italy on April 6, 2009 (Table 1). Despite the large amount of data collected (aftershock distribution, coseismic

cracks and focal mechanism) and interpretations made, several uncertainties persist about the deep geometry of the fault responsible for the L’Aquila earthquake and on the interpretation of rupture surface geometry associated with the earthquake.

Table 1. Main historical seismic events in the L’Aquila area [8].

MwM	Epicentral Area	Year
6.10	L’Aquila region	2009
5.02	L’Aquila region	1958
5.27	Mt. Gran Sasso	1951
5.7	Mt. Gran Sasso	1950
5.05	L’Aquila region	1916
5.33	L’Aquila	1791
6.67	L’Aquila region	1703
5.33	Monti della Laga	1672
5.33	L’Aquila region	1619
6.5	L’Aquila region	1461
5.56	L’Aquila region	1315

The aftershocks [9], focal mechanism [10], surface deformation detected from DInSAR [2,5,7], GPS measurement inversion [11], and coseismic surface cracks [12] do not converge on a single subsurface slip patch geometry for the L’Aquila earthquake [11,13–17]. Some studies suggest that the coseismic slip along the Paganica fault reached the Earth’s surface [14,18], while other studies infer that the rupture was blind [16]. Furthermore, aftershocks suggest the potential involvement of shallow-dipping thrust faults that may have been reactivated with normal slip [15,16].

In this research, using aftershocks’ locations associated with the L’Aquila 2009 earthquake [19,20] and coseismic cracks [12], we reconstructed five different slip surface configurations possibly associated with the seismic sequence (Table 2). The five plausible geometries are based on previous interpretations [13–16]; however, we reconstructed the three-dimensional fault geometries directly from both geologic and geophysical data.

Table 2. Two-dimensional (2D) vertical cross sections of five different fault configurations considered for the models. The dark blue normal faults have applied dip-slip shear stress drop of 1.5–4.5 MPa within the numerical models, the light blue faults freely slip in response to the main fault slip.

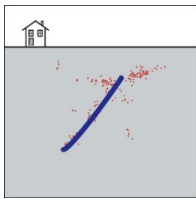
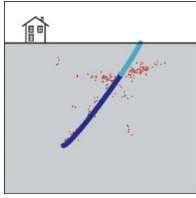
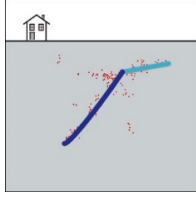
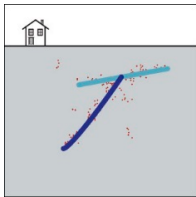
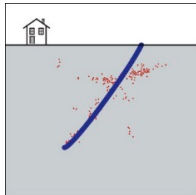
Cases	2D Section	Description
Case 1		Only the main blind normal fault.
Case 2		The main normal fault was extended to reach the surface coseismic ruptures [12]. This extension is independent from the main fault and represents a passive propagation towards the ground surface.
Case 3		The main normal fault is intersected at its upper tip by a low angle fault. This low angle fault is considered a thrust passively reactivated in extension only in the hanging wall of the main fault.

Table 2. Cont.

Cases	2D Section	Description
Case 4		The main normal fault interacts with and passively reactivates a low angle fault. For case 4 we propose a complete thrust passive extensional reactivation near the main faults.
Case 5		The main normal fault reaches the surface in correspondence of the coseismic ground ruptures.

We simulate coseismic deformation along these faults using forward three-dimensional boundary element method (BEM) models. One advantage of this approach over previously performed inversions is that the three-dimensional models incorporate non-planar fault configurations. We assess the sensitivity of slip patch geometry on the pattern of surface displacement, but due to the non-uniqueness of this assessment, we also consider the effect of host rock stiffness (Young's modulus) and coseismic stress drop on the ground deformation. We expect that increasing the applied stress drop increases the coseismic slip on the faults and the amplitude of surface displacement. In contrast, increasing host rock stiffness decreases fault slip and surface displacement. Consequently, we expect the models to have a trade-off in match to observation with lesser or greater stress drop and host rock stiffness. For this reason, we assess all five models through a range of reasonable stress drop and host rock stiffness parameter space. In order to constrain the subsurface coseismic slip surface configuration, we compare the surface displacements of the suites of models with line of sight measurements observed from DInSAR satellite [2]. The results of this sensitivity analysis show that the best fit between model results and observed surface deformation occurs for models where slip patch does not reach the surface; for these cases the numerical model results are consistent with the DInSAR displacements.

1.1. Study Area

The Apennines have a complex structure resulting from a long and composite geological history with the overprinting of different tectonic phases through time. The L'Aquila region was part of the African passive margin of the Ligurian-Piedmont Ocean in the Early Mesozoic, hosting wide carbonate platforms and pelagic basins that underwent the Triassic–Jurassic rifting [21,22]. The successive convergence between African and Eurasian plates began during the Cretaceous, leading to the formation of thrust systems and related foredeep basins that developed up to the Middle Pleistocene migrating towards the Adriatic Sea [23–26]. The core of central Apennines has been affected in the last ~2.5 Ma by SW-NE oriented extension, leading to normal faulting, that today characterizes the whole region [27–29]. Late Quaternary extensional faulting drives the development of shallow intermountain basins with a sediment thickness underneath L'Aquila of up to ~250 m (Figure 1) [30].

The current rate of overall extension in the central part of the Apennine, is 2–3 mm/year [31]. The L'Aquila earthquake occurred along the Paganica–S. Demetrio fault, which is one of the NW-SE striking normal faults that accommodates the Apennine extension [32,33]. One result of this overprinted tectonic history is that the older compressional structures can interact and possibly influence the surface deformation due to the currently active extensional faults in the central Apennines region [15,34].

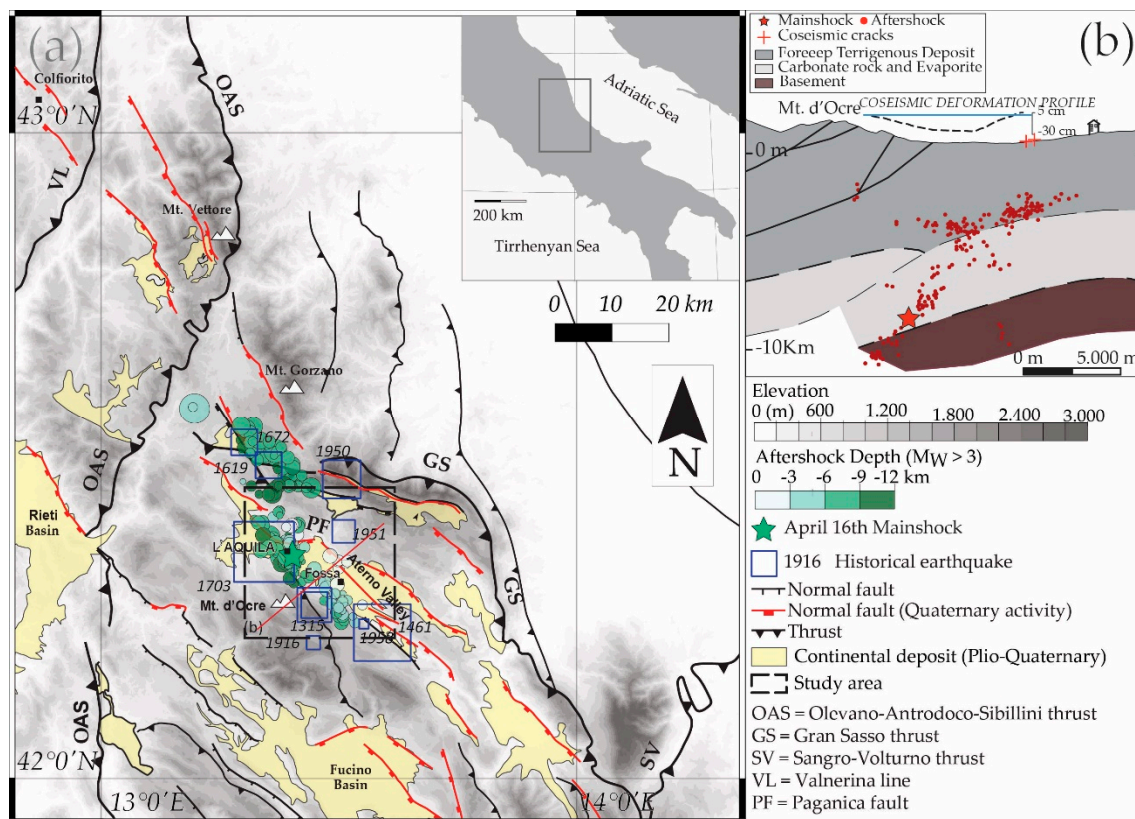


Figure 1. (a) Tectonic map of the central Apennines modified after [22] showing the positions of Quaternary intramountain basin and the main aftershocks. The axial part of the Apennines is dominated by thrusting and folding active between Upper Miocene and Middle Pleistocene, successively intersected by normal faults. (b) SW-NE geological section of the L'Aquila area modified after [16]. Relocated aftershocks [9], mapped coseismic cracks [12].

1.2. L'Aquila Seismic Sequence

On April 6, 2009 a Mw 6.3 earthquake struck the L'Aquila region as part of a long foreshock-aftershock sequence [9,19,20]. A dense local network composed of 67 three-component seismic stations detected the events; twenty of these stations are permanent stations of the Italian Seismic National Network (RSNC) and forty-seven were temporary stations installed after the mainshock to record the aftershock sequence [35]. Significant historical earthquakes in the region (Table 1 and Figure 1) occurred in 1461 ($M = 6.4$), 1703 ($M = 6.7$), and more recently in 1916 and 1958 [8,36]. Different interpretations were proposed for the geometry of the fault responsible of the 2009 event; most authors proposed a normal fault striking 130° – 135° N and dipping 45° – 55° toward SW with the lower tip at about 11–12 km below the surface (see [13] for a review). These reconstructions were carried out with various techniques using relocated aftershocks [19,20], GPS data inversion [11,37–39] or GPS and DInSAR inversion combined [2,5,7]. Field observations detected a localized network of small surface cracks (open fractures or minor dislocations) mainly along pre-existing faults [40]. The coseismic cracks were observed on three different non-continuous alignments with several gaps between sections of the crack zone, and the total zones' length was 13 km [12]. The most evident zone totaled 5–7 km in length along the northern part of the Paganica–S. Demetrio fault system [12]. Focal mechanisms confirm movement along a normal fault in agreement with the current extension tectonic regime of the area [10]. Most of the focal mechanism solutions of the aftershocks show a normal faulting in agreement with the tectonic setting of the area [10] and describe a fault with dip of about 50° and a strike of about $N135^{\circ}$ E [10].

2. Surface and Subsurface Data

To reconstruct the geometry of the faults responsible for the 2009 event in L'Aquila area, we combined available seismological and geological data: the aftershocks hypocentral distribution [9] and the surface coseismic cracks (Figure 2) [12]. We used the coseismic ground deformations detected from DInSAR as independent data to assess the predictions of the numerical models. Combining SAR deformation with the observed coseismic cracks is an approach successfully used in previous published work [41].

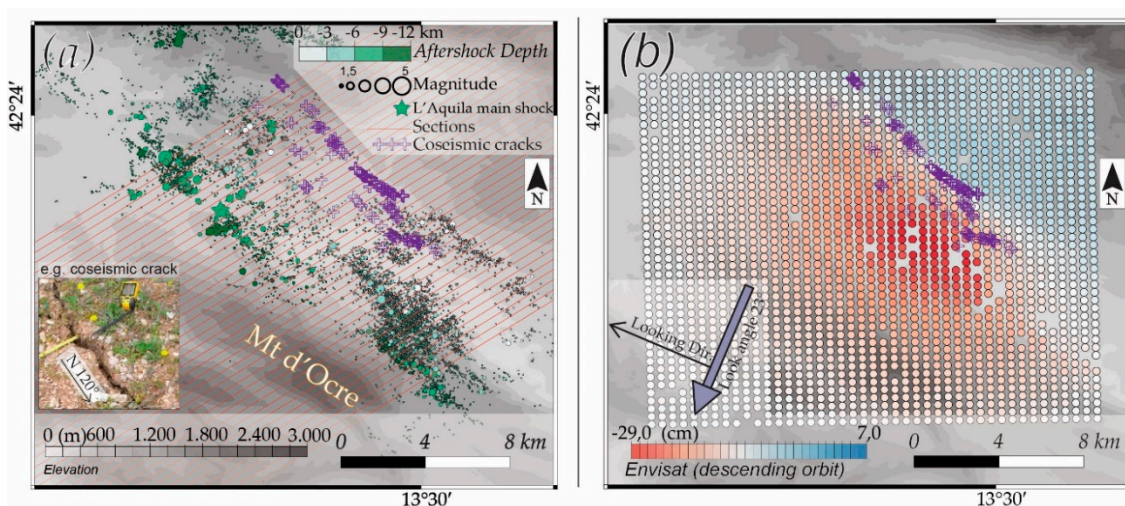


Figure 2. Digital elevation model of the study area with the projection of: (a) location and depth of the $M > 1.5$ aftershocks [9] and the coseismic cracks [12]; (b) coseismic surface line of sight displacements observed from Envisat (descending orbit).

2.1. Surface Data

Coseismic surface cracks affected an area of more than 100 km^2 around L'Aquila [12,40]. A set of 237 surface cracks were mapped within a 13-km-long zone that strikes between 130 and 140° N [12] and bounds a tectonic basin filled with Quaternary deposits [34,42]. Different types of ground deformations were mapped: coseismic fractures and surface deformation. Along the coseismic fractures, the observed slip varies between zero up to a few centimeters along fractures that dip between 60° and 80° , while measured openings vary between ~ 1 and 2.5 cm [12,43]. Coseismic cracks (Figure 2) were mapped along contacts between different near-surface lithologies. The differences in material properties, between poorly consolidated and unconsolidated alluvium, could possibly play a role in the development of the observed cracks [12].

DInSAR (differential SAR interferometry) techniques record the ground coseismic deformation in the direction of the satellite look angle (e.g., [1]). Here, we used the Envisat data (descending orbit) published by Atzori et al. [2] to constrain between alternative subsurface coseismic slip patch configurations. Using the April 27, 2008–April 12, 2009 pair acquired descending Envisat orbit (right look angle of 23° and 41 m perpendicular baseline) integrated with GPS data [2], we determined the coseismic ground deformation associated with the L'Aquila earthquake. This interferogram does not show deformation except for the L'Aquila event and is consistent with the interferograms (Envisat ascending and CosmoSkymed ascending) published by Atzori [2]. The maximum observed line of sight displacement occurred between the cities of L'Aquila and Fossa with movement away from the satellite of up to 29 cm [2]. The DInSAR analysis did not show a sharp change in displacement that would indicate a shallow slip [2]. If the fault rupture breaks the ground surface we would expect maximum surface displacement along the fault, which would produce maximum and minimum line of sight displacements very near to the fault trace. Instead, the minimum and maximum are separated by $5\text{--}6 \text{ km}$. For this reason, several of the best-fitting inversions to the DInSAR data have little slip along

the Paganica fault near the Earth's surface [5]. The area of maximum deformation measured by the interferogram (Figure 2) does not correlate with the position of the coseismic cracks [44]. Furthermore, small-wavelength displacement anomalies associated with coseismic cracks show local lowering up to a few centimeters [44], however this local subsidence does not influence the longer wavelength displacement across the area [44]. This local subsidence near surface cracks is an order of magnitude lower than the larger-scale subsidence in the hanging wall of the fault and is also very localized [12].

2.2. Aftershock Data

A catalogue of more than 50,000 relocated aftershocks [9], spanning from April to December 2009, was used to reconstruct plausible fault configurations (Figure 3).

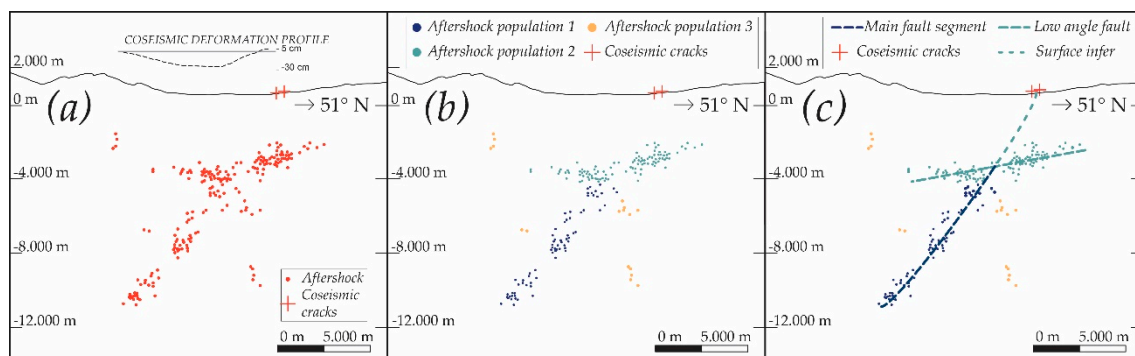


Figure 3. Cross section showing (a) aftershocks distribution [9] and coseismic cracks [12]; (b) different populations of aftershocks are shown in dark and light blue; (c) possible coseismic fault geometries interpreted to fit the data. The interpretation of the L'Aquila main fault segment was based on aftershock population 1 (dark blue); population 2 (light blue) was associated with a shallow low angle secondary fault and population 3 was associated with minor structures. The surface projection connects the main fault upper tip to the coseismic surface cracks.

Aftershocks, between 4 and 11 km in depth, appear aligned along a sub-planar surface dipping 50° – 55° to the SW and extending 17–18 km in a NW-SE direction. The rock volume affected by the aftershocks varies in width along strike from 0.3 to 1.5 km [9]. The estimated median error for aftershock distribution is 0.024 km on X easting axis, 0.015 km on Y northing axis, and 0.027 on Z vertical axis km, while the mean errors are 0.178, 0.039, and 0.087 km, respectively [9]. The aftershocks primarily occur between 4 and 10 km in depth; only very few events occur between the surface and 2 km in depth or below 12 km [9,19,20,45]. Over 80% of aftershocks, including major events, are deeper than 4 km [44], which suggests that rupture may not have extended to shallow depth. Between 3 and 12 km of depth many aftershocks align along a sub-planar surface dipping 50° – 55° to the SW and striking NW-SE. We recognized this cluster (population 1) throughout the study area. Between 2 and 4 km depth, a second population of aftershocks (population 2) are aligned along a sub-planar surface dipping $\sim 10^{\circ}$ to the SW and extending in the NW-SE direction. Population 2 is composed of less events than population 1, despite being clearly recognized all along the study area. Lastly, some aftershocks are grouped in small clusters lacking lateral continuity (population 3). These small clusters do not occur in continuity with the main fault and were too small to be connected to significant tectonic structures. For these reasons, population 3 will not be considered in our interpretation (Figure 3). The large number of aftershocks within the days following the mainshock do not show a migration of the aftershock spatial distribution. Aftershocks are evenly distributed between high-angle and low-angle fault lines over the time of the observation. For this reason, we use all of the aftershock dataset, in order to better constrain the faults geometries (Figure 4).

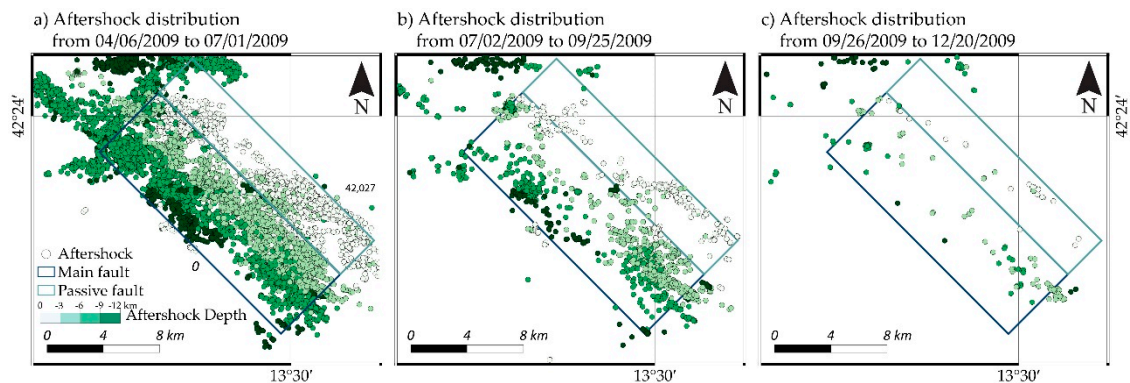


Figure 4. Maps view of the aftershock distribution from 04/06/2009 to 12/20/2009. While the number of aftershocks decreases over time, there is no significant evolution of the spatial distribution of the shocks.

3. Methodology

3.1. Fault Construction

We have collected and geo-referenced the available aftershock data using MoveTM software (Petroleum Experts). Observing aftershock distribution, we have reconstructed two fault surfaces: the main surface from aftershock population 1 and a secondary fault from population 2 that at shallower depths, has similar strike but a lower dip. We projected aftershocks and ground cracks into forty cross sections, 500 m laterally spaced and perpendicular to the orientation of the aftershock distributions, which is about 130° N, a trend very close to the alignment of the coseismic crack zone. The aftershock population 1 (Figure 3), which is conspicuous all along the study area, constrained our three-dimensional (3D) reconstruction of the Paganica fault plane responsible for the L'Aquila earthquake [2,46]. On each section, we manually selected the aftershocks belonging to population 1 and, using a linear regression automatic fitting tool, which estimates the fault segment using the average position of each aftershock population, we traced a 2D fault segment representing the best fit of the aftershocks.

Interpolation of all the reconstructed segments led to a three-dimensional fault surface representing the portion of the Paganica fault that slipped during the L'Aquila earthquake. This constructed fault surface is sub-planar and extends from 3 to 11 km in depth with a total along strike length of 18 km, overall strike of 130° – 135° and dip of 50° – 55° towards the SW. We applied the same approach to construct a three-dimensional secondary fault surface from the aftershock population 2 (Figure 3). The fault plane strikes 130° – 135° , parallel to the main one and shows a gentle dip (10°) towards the SW. We also reconstructed a third fault representing the potential connection of the main fault to the surface. To do this, we connected the upper tip of the main and the coseismic cracks mapped on the ground surface (Figure 5).

We use these three fault surfaces to assess the role of the following five different plausible fault configurations on coseismic ground deformation (Figure 5):

- Case 1 considers only the main blind normal fault extending from 3 to 11 km of depth;
- Case 2 includes the main fault and its prolongation up to the coseismic cracks mapped by Boncio et al. [12]. This model explores the possibility that coseismic slip along the main fault gives passive deformations along the third fault;
- Case 3 includes the main fault and a portion of the shallower low angle secondary fault. This configuration follows the reconstructions by Bigi et al. [15] and Valoroso et al. [9] that show a pre-existing thrust fault reactivated in extension only in the footwall of the main fault;
- Case 4 considers the main fault and the entire shallower low angle fault. This case follows reconstructions by Bonini et al. [16] that suggest a complete extensional reactivation of the thrust both in the hanging wall and in the footwall of the main fault;

- Case 5 is geometrically coincident with Case 2, but here the plane connected to the surface is not passively activated but it is part of the main fault plane reaching the surface. In this case we follow the conceptual model proposed by [14] where the main normal fault reaches the surface and the coseismic ground cracks are directly connected with the fault responsible for the L'Aquila earthquake.

The faults are not perfectly planar and show along strike variations. These faults are consistent with other reconstructions based on focal mechanism solutions [10], aftershock locations [13,16] and geological observations on the Gorzano fault [5,7,15]. Since no aftershocks were detected in the first km of depth [9,41], we have not considered cases with faults terminated just beneath the surface.

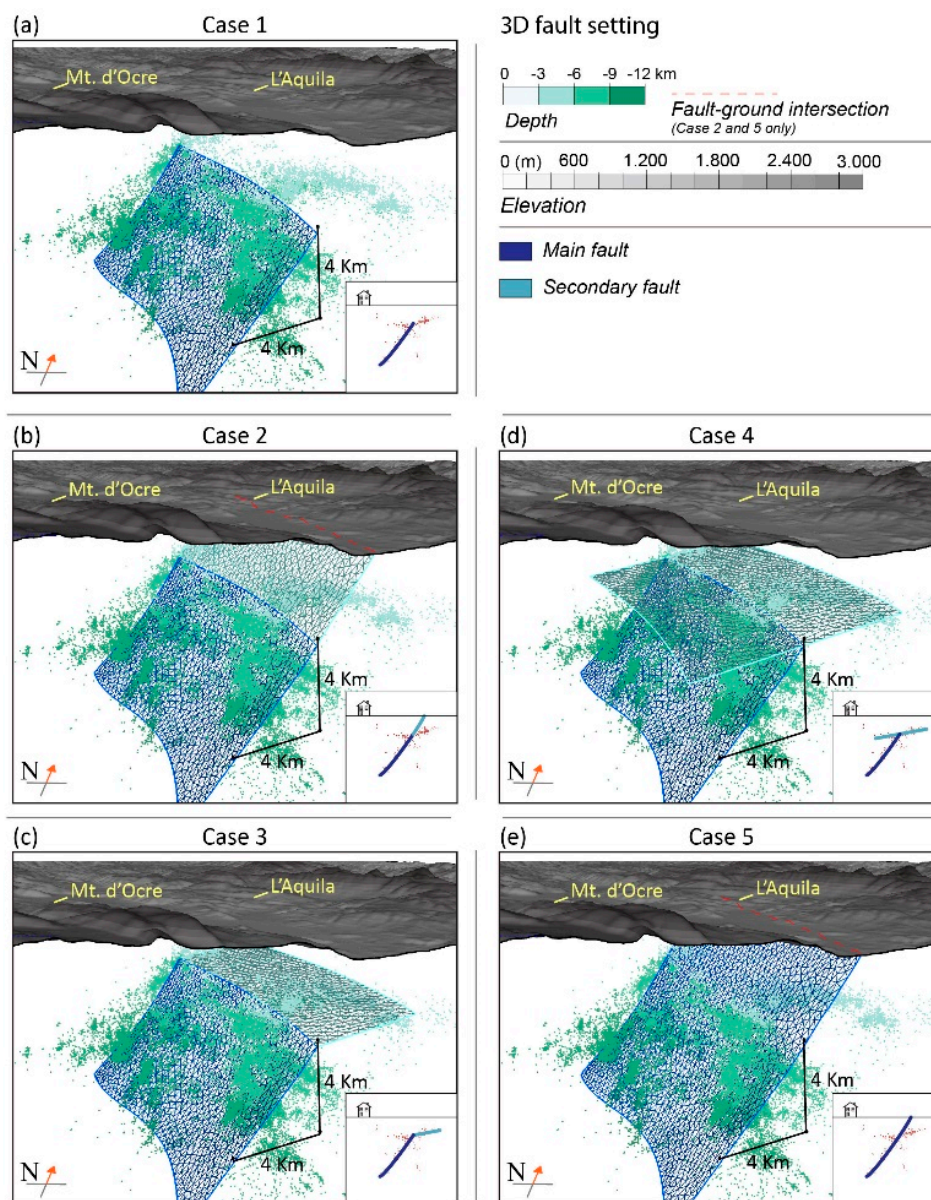


Figure 5. 3D view of the five fault configurations of the numerical models with (in green) the aftershock cloud. (a) Case 1: blind active normal fault (dark blue); (b) case 2: blind active normal fault with an passive (light blue) extension to the ground surface (red line); (c) case 3: blind active normal fault with a passive thrust in the footwall; (d) case 4: blind active normal fault with a passive thrust in both foot and hanging wall; (e) case 5: active normal fault reaches the ground surface.

3.2. Numerical Models

We used numerical models to simulate the surface coseismic deformation of the L'Aquila earthquake associated with the five plausible fault interpretations and compared the resulting ground deformation to line of sight coseismic displacements observed by Envisat satellite. The simulations use Poly3D, a three-dimensional BEM software based on triangular fault elements that allow accurate deformation along non-planar faults [47]. Poly3D has been used to investigate the mechanics of, and interactions among, three-dimensional faults (e.g., [48–53]). Poly3D solves the relevant equations of continuum mechanics to calculate stress and displacements throughout the model [47]. The algebraic expressions for the elastic fields around each element are derived by superposing the solution for an angular dislocation in an elastic half-space [54,55] in the way described by Brown [56] and Jeyakumaran [57]. Stresses and displacements can be reported on both faults and arbitrary observation surfaces. Within Poly3D, faults are discretized within a linear-elastic homogeneous half-space. Poly3D fault models have successfully simulated coseismic surface deformation associated with slip along fault surfaces (e.g., [51,58,59]). For the models of this study, we meshed the fault surfaces (Figure 5) within Poly3D with triangular elements whose sides are 500 m.

For the numerical experiments, we prescribe each fault surface as either active and passive. In the models, active faults that produce L'Aquila mainshock prescribed shear stress drop. Following the approach of Madden and Pollard [51] for simulating coseismic deformation of the Landers 1992 earthquake, we applied a shear traction to the active faults that corresponds to the average shear stress drop of the earthquake. In the models here, in order to simulate the L'Aquila mainshock, we applied dip-slip shear traction to active faults. In contrast, passive faults are those that slip in response to the mainshock [60]. In the numerical models, the passive faults are free to slip (prescribed zero shear traction) in response to the stress drop on the active fault. In cases 1 and 5, a single fault plane is present; for cases 2, 3 and 4, the L'Aquila fault remains active while all the other fault surfaces respond passively (Figure 5). In our models, the passive faults are prescribed to be freely-slipping ($\tau = 0$) so that they slip in response to slip along the normal fault that has applied stress drop. The geological sections available for the area show homogeneous lithologies mostly composed by dolomitic and calcareous deposits, these lithologies have similar stiffnesses with depth [44]. The amount of coseismic surface deformation depends not only on fault geometry but also on values for coseismic stress drop and effective elastic stiffness of the host rock. We test the sensitivity of all five cases to both stress drop and material stiffness. The average stress drop associated with the L'Aquila earthquake was determined using acceleration and velocity waveforms as 2.6 MPa [61], the bulk of the observations varying between 1 and 5 MPa [61]. To encompass a range of potential values, we varied the stress drop from 1.5 to 4.5 MPa. Trasati et al. [7] used the velocity structure of the region to infer a Lamé lambda constant of 30 GPa and shear modulus of 18 GPa for the upper few km and Lamé constant of 50 GPa and shear modulus of 30 GPa below 10 km depths. From these values, we calculated Young's modulus ranging from 47 to 80 GPa. Other researchers proposed lower stiffness values for sedimentary rocks, between 20 and 45 GPa (e.g., [62]). Due to the wide range in estimated stiffness, we tested a wide range of stiffness values from 20 to 80 GPa and used Poisson's ratio of 0.25 [5,7]. In total, we performed 245 models by testing five different fault configurations, seven stress drop values and seven stiffness values.

3.3. Line of Sight (LOS) Correction

Each numerical model produces ground deformation associated with the simulated coseismic stress drop. We sampled the model surface deformation at the locations of satellite data information [2]. While the models produced complete three-dimensional displacement fields with east, north and up displacements, the DInSAR data only provided line of sight (LOS) information along the look angle of the satellite. We converted the displacements resulting from the numerical models to the satellite line

of sight (LOS) considering both satellite right look angle and satellite 23° direction (Coef. Est, Coef. North and Coef. Up) provided by Atzori [2] and using the formula:

$$\text{LOS} = \Delta u_{\text{east}} * \text{Coef. East} + \Delta u_{\text{north}} * \text{Coef. North} + \Delta u_{\text{up}} * \text{Coef. Up}, \quad (1)$$

We assessed the viability of the previously described five cases by comparing the ground deformation patterns from satellite observations and those resulting (and corrected) from model simulations.

4. Results

To compare the numerical model predictions to the observed ground deformation we subtracted the DInSAR surface displacements from the LOS Poly3D displacements for all the tested fault configurations (Figures 6–8. See supplementary materials). For each fault configuration (Figure 7), we showed the different maps for the range of tested stress drop and stiffness (Figure 8) and also showed the median of the net difference maps (absolute value of model – absolute value of observed). For the L'Aquila earthquake, the dominant signal in the ground displacements was away from the satellite movement of the ground surface above the hanging wall of the normal fault (negative displacement Figure 6a). The DInSAR also showed a minor deformation towards the satellite ground surface movement of the ground in the footwall of the normal fault.

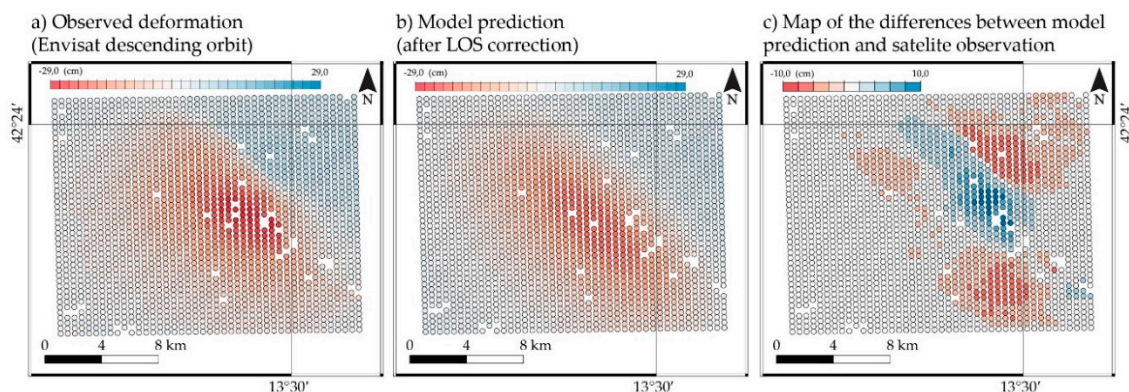


Figure 6. Maps showing the conceptual scheme used to calculate the differences between the observed and the modeled surface line of sight (LOS) displacements.

4.1. Residual Difference Maps

The comparison between the predicted (model) and observed DInSAR displacements calculated along the line of sight (LOS) of the satellite highlight how fault configurations, stress drop and stiffness affect the surface deformation (Figure 7).

Within Figure 7, negative values indicate regions either where the model towards the satellite displacement is less than observed or where model ground displacement away from the satellite is greater than observed.

Case 1 (blind normal fault, Figure 7a): Since the away from satellite displacement of the ground above the normal fault's hanging wall dominates the displacement pattern (Figure 6a), we will focus the comparison of case 1 surface difference maps to this aspect of the deformation. High stiffness in the models reduce the away from satellite deformation of the ground above the hanging wall of the normal fault. Displacement maps of models with high stiffness in Figure 7a have the greatest positive (blue) difference. In contrast, increasing stress drop increases the away from satellite ground displacement above the hanging wall and increasing the stress drop produces more negative difference maps (red). The best match (i.e., models with low differences between model and satellite observations), are those that cross Figure 7a from the upper right to the bottom left where the trade-offs of stiffness and stress

drop are balanced. Among these results are models where stress drop values are close to the values inferred for earthquakes similar to the L'Aquila one (2.5–3 MPa) [61,63].

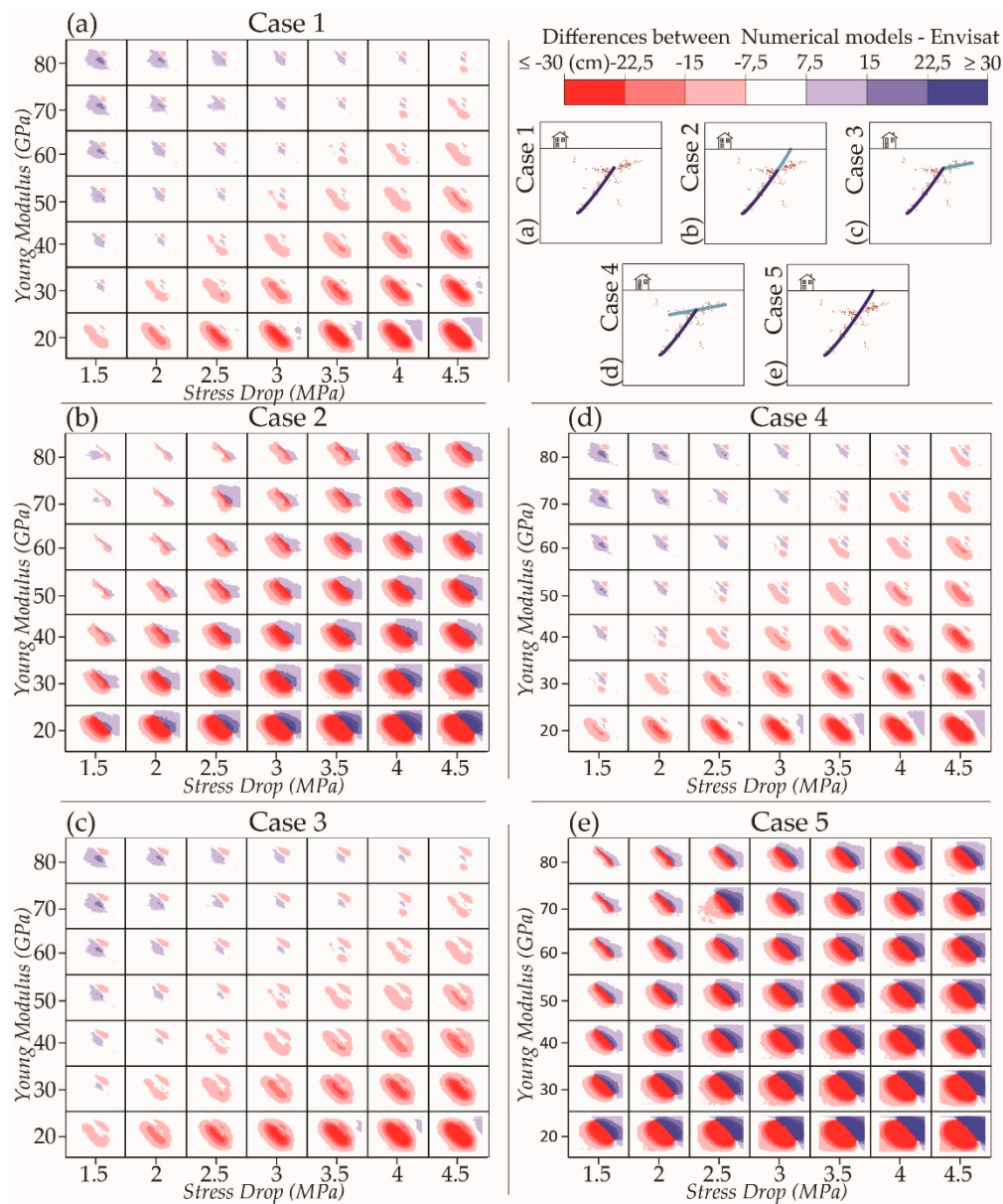


Figure 7. Maps of the residual differences between numerical models and satellite observed surface line of sight displacements as calculated in Figure 5. The color scale has been limited to between +20 and −20 cm, and the white area represents a differential deformation <7.5 cm. Subfigures from (a–e) represents a two-dimensional (2D) vertical cross sections of the five different fault configurations.

Case 2 (main fault with passive connection to surface, Figure 7b): The model results show the same trends for increasing stress drop and stiffness as case 1, but the balance between the two parameters is reached with minimum mismatch at a relatively low stress drop and high values of stiffness. According to published data [61], these values may not be representative of this earthquake. Increasing the applied stress drop from 1.5 MPa increases both the away from satellite ground movement in the hanging wall and the towards the satellite movement of the footwall of the normal fault. This outcome is consistent with a greater normal slip on the fault that would increase the downdrop of the footwall and uplift of the hanging wall.

Case 3 (main fault and secondary fault within footwall, Figure 7c): The results show a pattern of residual deformation comparable with case 1. A comparison between case 3 and 1 reveals that the presence of the low-angle secondary fault has a small impact on the surface deformation above the footwall region. Slip along the shallower low angle fault in response to stress drop along the main one reduces the towards the satellite ground deformation in the footwall of the main fault. This result is consistent with normal dip-slip along the secondary fault that would pull the overlying rock volume downward relative to case 1 that has no secondary fault.

Case 4 (main fault and complete secondary fault, Figure 7d): The results show a differential deformation pattern comparable to case 1 (Figure 7d). At the surface, deformation above the footwall more closely resembles case 1 than case 3, suggesting that the secondary fault slips differently if it extends through both the hanging wall and footwall of the main fault (instead of being limited to the footwall, as in case 3). In case 4, the dip-slip is focused on the portion of the secondary fault in the hanging wall of the main fault. For example, the maximum slip in the model with 3 MPa of stress drop and 50 GPa of stiffness, is 0.35 m in the hanging and 0.16 m in the footwall. Also, the main fault slips more (up to 1.15 m) in case 4 than in either case 1 or 3 (respectively, up to 1.0 and 1.1 m). For models with equal stress drop and stiffness in cases 3 and 4, the model of case 4 produces slightly greater mismatch to satellite observation than case 3.

Case 5 (stress drop applied to a single main fault plane reaching the surface, Figure 7e): The resulting difference maps resemble those of case 2 with even greater away from the satellite ground displacement of the footwall. This outcome is consistent with the greater fault slip as stress drop is applied to a unique outcropping fault plane. The best match of surface displacement within the range of parameters tested is with the lowest stress drop and highest stiffest host rock; however, this difference map does not show as close a match of model and observation as the models with other active fault configurations.

4.2. Median Net Difference

To assess the overall match of each model with variations of stress drop and stiffness, Figure 8 shows the median difference between the absolute values of the calculated model and the observed displacements.

The use of absolute values of the displacement ensures that areas of positive and negative displacement do not offset one another. While the resulting mismatch values have a very wide range, to better highlight the results with the closest match to satellite observation we limited the color scale to between +20 and -20 cm. The white colors represent net differences lower than 4 cm, indicating the best match between numerical results and observed DInSAR displacements. The purple colors indicate numerical models with median net displacement (both towards and away from the satellite) that exceeds the DInSAR, while the orange colors indicate numerical models with median net displacement that underestimate the DInSAR. Increasing stress drop and decreasing stiffness both increase the ground surface displacements in the numerical models (Figure 8). In all diagrams of Figure 8 the upper left cases (high stiffness and low stress drop) underestimate the median observed displacements, while the lower right cases (low stiffness and high stress drop) overestimate the surface deformation.

Cases 1, 3 and 4 (blind faults, Figure 8a,c,d) show similar distribution of net difference values. The models that show minimum differences are those with a stress drop of 3 MPa and 50 GPa stiffness. In case 5 (outcropping fault) only models with a stress drop of 1.5 MPa and a stiffness of 80 GPa approximate the surface deformations. Case 2 presents results similar to case 5 with the best models' results associated with low stress drop and high stiffness values.

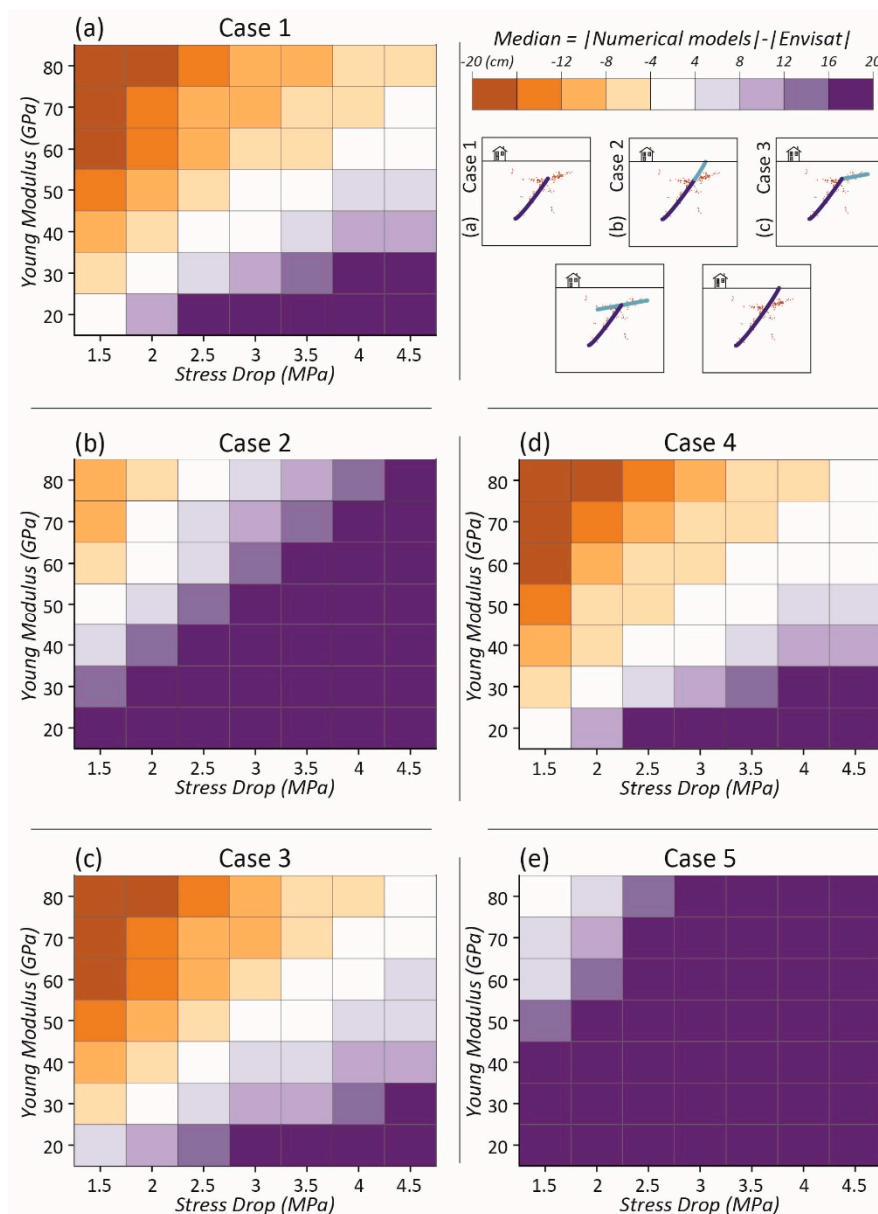


Figure 8. Differences diagram showing the median absolute difference of LOS deformation between numerical models and satellite observation. Subfigures from (a–e) represents a two-dimensional (2D) vertical cross sections of the five different fault configurations.

5. Discussion

The L'Aquila earthquake, which may have involved slip on several different fault surfaces, may be an example of deformation within early phases young extensional regimes that could involve also pre-existing inherited structures [64]. Despite the wide amount of data collected on the L'Aquila earthquake, multiple subsurface slip surface interpretations persist. All the reconstructions agree that the L'Aquila seismic sequence was primarily caused by slip along the Paganica normal fault, striking 130° – 135° N with the lower tip of the fault plane at 11–12 km in depth [13]. At shallower depths a wide range of possible slip surface geometries have been proposed [2,14–16]. For example, some proposed slip along a sub-horizontal inherited structure triggered by the interaction with the slip along the main normal fault [15,16], while other studies suggested that the slip propagation on the Paganica fault during the L'Aquila earthquake reached Earth's surface without any interaction with inherited structures [14,18]. The numerical models of this study assess the different slip surface

geometries proposed by different authors by comparing the numerical results to independent data on surface ground movement from DInSAR. The numerical results show that, for the range of stress drop and stiffness tested here, models with blind normal faults (cases 1, 3 and 4) better approximate the observed ground deformation [2] than models where faults directly outcrop to the surface (cases 2 and 5; Figure 9).

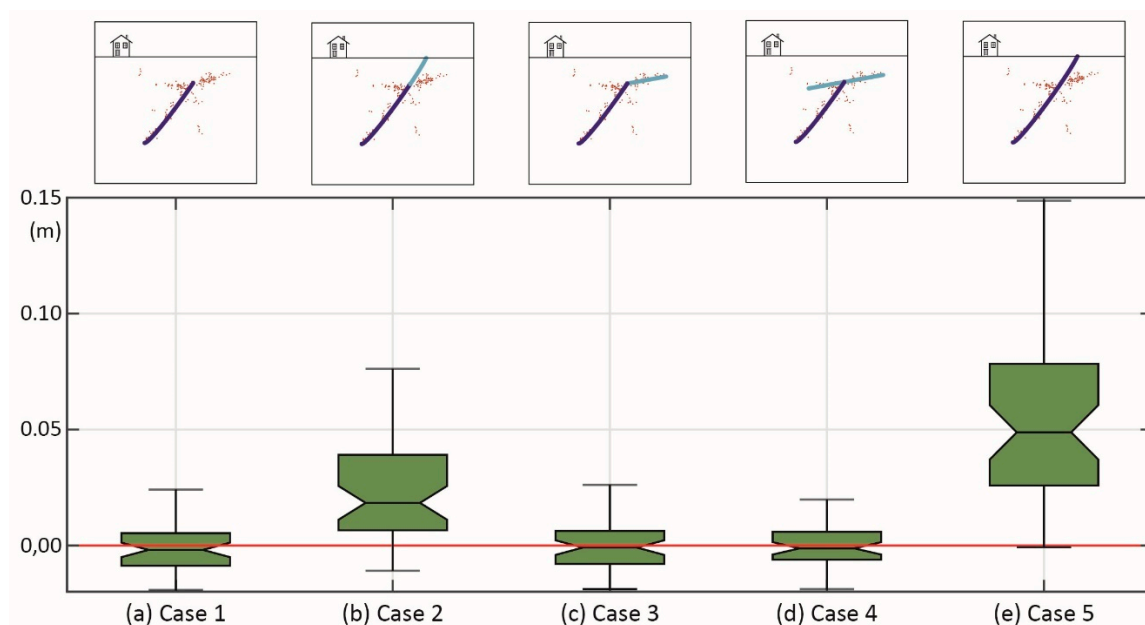


Figure 9. Median mismatch, calculated from different maps, for the five considered geological settings. Horizontal black mark indicates the median value; bars are extended on the whole data range from the minimum to the maximum value; the bottom and top edges of the green area indicate the 25th and 75th percentiles, respectively. The red line indicates zero differences between observed and predicted ground deformation.

The models incorporating an outcropping fault (either passive, case 2, or active, case 5) only reproduce the observed coseismic displacements for a narrow range of stress drop and stiffness that are at or near the bounds of the permissible ranges [7,61,62]. For case 5 (Table 3), the only simulation consistent with the observed surface deformation occurs with 80 Gpa host rock stiffness and 1.5 MPa stress drop (Figure 8), however this stress drop is smaller than that estimated for the L'Aquila earthquake of 2.6 MPa [61]. The models with an outcropping fault seem to not match the surface displacements because the DInSAR data do not show a sharp discontinuity in ground displacements across the projected fault surface traces, and minimum and maximum ground deformation values (−29 and +7 cm) are separated by 5–6 km [2]. The models with a blind fault are consistent with previous inversions from the DInSAR data which show little or no slip from the upper few kilometers [5,7].

Table 3. Summary of the characteristics of the best results obtained for the different geometries.

Case	Stress Drop	Rock Stiffness	Maximum Slip	Seismic Moment
Case 1	3.0 MPa	50 GPa	1.0 m	2.5×10^{18} Nm
Case 2	2.5 MPa	80 GPa	0.8 m	4.0×10^{18} Nm
Case 3	3.0 MPa	50 GPa	1.1 m	3.0×10^{18} Nm
Case 4	3.0 MPa	50 GPa	1.2 m	2.9×10^{18} Nm
Case 5	1.5 MPa	80 GPa	0.8 m	4.4×10^{18} Nm

These findings seem to suggest that the fault rupture could have been blind and that both the surface cracks mapped [12] and the observed post-seismic deformation [65] may not reflect coseismic

rupture to the Earth's surface. Post-seismic deformation [65] could include secondary gravitational effects and may not be a direct expression of slip propagation to the ground surface. The good match of numerical models that incorporate blind faults (cases 1, 3 and 4) suggests that an active fault buried 3 km below the surface can replicate ground deformation during the 2009 L'Aquila earthquake. A triggered slip along a synthetic low-angle fault, detected from aftershock distribution, locally impacts the coseismic surface deformation within the footwall [16]; however, this footwall deformation is much smaller than the hanging wall displacements.

We can test if the best fitting models also produce maximum slip and seismic moment that are consistent with observed source parameters and with previous interpretations (Table 4). In addition to the average stress drop value for the L'Aquila earthquake of 2.6 MPa [61], the maximum amount of slip on a fault surface is ~1 m [13] and seismic moment is between 2.9 and 3.5×10^{18} Nm [2,38]. For cases 1 and 3 (Table 3), models with 3 MPa stress drop and 50 GPa Young's modulus, that have a good match to the observed ground displacement, produce maximum slip of ~1 m and seismic moment between 2.5 and 3.0×10^{18} Nm corresponding to a 6.3 moment magnitude. The slip amount and observed ground deformation resulting from this model are consistent with observations [2,38]. For case 4, the model with 3 MPa of stress drop and 50 GPa of Young's modulus has good match to the observed ground displacement and the seismic moment is 2.9×10^{18} Nm corresponding to a 6.3 moment magnitude. However, the maximum slip value in this model reaches 1.15 m. It is interesting that this model produces more slip but the same seismic moment. For case 2 (Table 3), the model with 2.5 MPa stress drop and 80 GPa stiffness has good correspondence with observed deformation; however, the maximum fault slip is 0.75 m and seismic model is 4.0×10^{18} Nm. While the slip values are lower than those of other models, the seismic moment exceeds both the values from other models and estimates of seismic moment [2,13,38]. Cases 2 and 5 have greater areas of coseismic slip so that even with lesser maximum dip-slip magnitude, the total seismic moment over-predicts the estimates for seismic moment of the L'Aquila earthquake [2,38].

Table 4. Summary of the main features of the L'Aquila fault; see [13] for a review.

Author	Maximum Slip	Seismic Moment	Strike	Dip
Atzori et al., 2009 [2]	90 cm	2.90×10^{18} Nm	133°	47°
Cheloni et al., 2010 [39]	100 cm	3.90×10^{18} Nm	135°	50°
Cirella et al., 2009 [38]	110 cm	3.50×10^{18} Nm	133°	54°

Although triggered slip (up to 0.35 m) along the secondary low-angle fault does not greatly affect the coseismic surface displacements, the aftershocks distribution suggests two distinct faults [15,16]. Consequently, case 3 (Figure 10) which includes the low-angle secondary fault both matches the ground displacements and honors the aftershock pattern. Interestingly, the upper tip of the main fault has the same depth where Bigi et al. [15] placed a sub-horizontal fault. According to Bonini et al. [16] the upper tip of the L'Aquila rupture patch coincides with a remarkable discontinuity which can be interpreted as a thrust plane [16]. Aftershock alignments, focal mechanisms and receiver function analyses also highlight a lithological change associated with a discontinuity striking N 334° and dipping about 20° towards SW at 3–4 km depth [16].

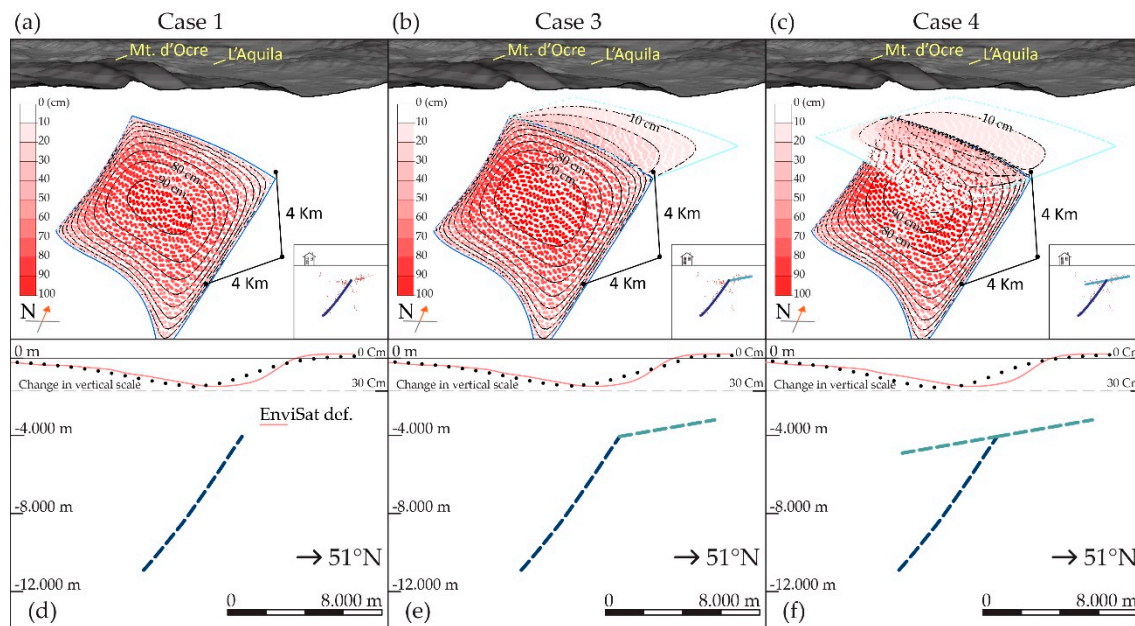


Figure 10. Slip distribution for (a) case 1, (b) case 3 and (c) case 4 with 3 MPa stress drop and 50 GPa Young's modulus. The cross-sections of (d–f) show the vertically exaggerated observed ground deformation (red line) [2] and the numerical models results (black dots) for our preferred cases.

6. Conclusions

We ran numerical models in order to execute a sensitivity analysis on five different 3D fault configurations by varying both stress drop and material stiffness. In our simulations, we also considered the potential influence of coseismic slip along a low angle inherited fault structure on ground deformation. According to our numerical models results, our preferred interpretation is that the L'Aquila earthquake activated a deep section of the Paganica fault causing only a little slip along faults near the Earth's surface. It also seems plausible that a blind normal fault triggered a local slip along a low-angle structure located around 3–4 km in depth.

The coseismic cracks are aligned along the surface expression of the Paganica fault; however, the model results from this study suggest that the slip of the 2009 L'Aquila earthquake remained mostly blind. Here we show that the best fits between DInSAR observation, and numerical simulation suggests that coseismic ground displacements do not seem to be a direct expression of fault slip at the Earth's surface in the L'Aquila 2009 earthquake. The numerical models' results also highlight (Figure 9) how fault geometry controls surface deformation pattern.

Supplementary Materials: The following are available online at <http://www.mdpi.com/2076-3263/9/9/370/s1>, Table S1: Case 1.

Author Contributions: Created the geological model, performed the numerical models and elaborate raw data, Y.P., M.L.C. and G.T.; conceptualized the study, developed the methodology and prepared the initial draft, Y.P., G.T. and M.L.C.; supervised and provided critical reviews and editing, M.L.C., G.T., S.S. and C.P.

Funding: This research received no external funding.

Acknowledgments: Many thanks to Simone Atzori (INGV national earthquakes center, Rome) for providing DInSAR data. Many thanks also to Luisa Valoroso (INGV national earthquakes center, Rome) for providing the aftershock data. The research period at the University of Massachusetts, Amherst was funded by the University of Pavia, Italy, Bando Mobilità Internazionale. Petroleum Experts Ltd. is kindly acknowledged for providing the MOVE Suite licenses to the University of Pavia. Schlumberger Ltd. is kindly acknowledged for providing the Poly3D to the University of Pavia.

Conflicts of Interest: The authors declare no conflicts of interest.

References

1. Massonnet, D.; Rossi, M.; Carmona, C.; Adragna, F.; Peltzer, G.; Feigl, K.; Rabaute, T. The displacement field of the Landers earthquake mapped by radar interferometry. *Nature* **1993**, *364*, 138–142. [[CrossRef](#)]
2. Atzori, S.; Hunstad, I.; Chini, M.; Salvi, S.; Tolomei, C.; Bignami, C.; Stramondo, S.; Trasatti, E.; Antonioli, A.; Boschi, E. Finite fault inversion of DInSAR coseismic displacement of the 2009 L'Aquila earthquake (central Italy). *Geophys. Res. Lett.* **2009**, *36*. [[CrossRef](#)]
3. Chini, M.; Atzori, S.; Trasatti, E.; Bignami, C.; Kyriakopoulos, C.; Tolomei, C.; Stramondo, S. The May 12, 2008, (Mw 7.9) Sichuan Earthquake (China): Multiframe ALOS-PALSAR DInSAR analysis of coseismic deformation. *IEEE Geosci. Remote Sens. Lett.* **2010**, *7*, 266–270. [[CrossRef](#)]
4. Stramondo, S.; Cinti, F.R.; Dragoni, M.; Salvi, S.; Santini, S. The August 17, 1999 Izmit, Turkey, earthquake: Slip distribution from dislocation modeling of DInSAR and surface offset. *Ann. Geophys.* **2002**, *45*, 527–536.
5. Walters, R.J.; Elliott, J.R.; D'Agostino, N.; England, P.C.; Hunstad, I.; Jackson, J.A.; Parsons, B.; Phillips, R.J.; Roberts Edinburg, G. The 2009 L'Aquila earthquake (central Italy): A source mechanism and implications for seismic hazard. *Geophys. Res. Lett.* **2009**, *36*, L15305. [[CrossRef](#)]
6. Wang, X.; Liu, G.; Yu, B.; Dai, K.; Zhang, R.; Chen, Q.; Li, Z. 3D coseismic deformations and source parameters of the 2010 Yushu earthquake (China) inferred from DInSAR and multiple-aperture InSAR measurements. *Remote Sens. Environ.* **2014**, *152*, 174–189. [[CrossRef](#)]
7. Trasatti, E.; Kyriakopoulos, C.; Chini, M. Finite element inversion of DInSAR data from the Mw 6.3 L'Aquila earthquake, 2009 (Italy). *Geophys. Res. Lett.* **2011**, *38*, L08306. [[CrossRef](#)]
8. Rovida, A.; Locati, M.; Camassi, R.; Lolli, B.; Gasperini, P. *CPTI15, the 2015 Version of the Parametric Catalogue of Italian Earthquakes*; Istituto Nazionale di Geofisica e Vulcanologia: Rome, Italy, 2016; pp. 1–33.
9. Valoroso, L.; Chiaraluce, L.; Piccinini, D.; Di Stefano, R.; Schaff, D.; Waldhauser, F. Radiography of a normal fault system by 64,000 high-precision earthquake locations: The 2009 L'Aquila (central Italy) case study. *J. Geophys. Res. Solid Earth* **2013**, *118*, 1156–1176. [[CrossRef](#)]
10. Scognamiglio, L.; Tinti, E.; Michelini, A.; Dreger, D.S.; Cirella, A.; Cocco, M.; Mazza, S.; Piatanesi, A. Fast Determination of Moment Tensors and Rupture History: What Has Been Learned from the 6 April 2009 L'Aquila Earthquake Sequence. *Seismol. Res. Lett.* **2010**, *81*, 892–906. [[CrossRef](#)]
11. Serpelloni, E.; Anderlini, L.; Belardinelli, M.E. Fault geometry, coseismic-slip distribution and Coulomb stress change associated with the 2009 April 6, M_w 6.3, L'Aquila earthquake from inversion of GPS displacements. *Geophys. J. Int.* **2012**, *188*, 473–489. [[CrossRef](#)]
12. Boncio, P.; Pizzi, A.; Brozzetti, F.; Pomposo, G.; Lavecchia, G.; Di Naccio, D.; Ferrarini, F. Coseismic ground deformation of the 6 April 2009 L'Aquila earthquake (central Italy, M_w 6.3). *Geophys. Res. Lett.* **2010**, *37*, L06308. [[CrossRef](#)]
13. Vannoli, P.; Burrato, P.; Fracassi, U.; Valensise, G. A fresh look at the seismotectonics of the Abruzzi (Central Apennines) following the 6 April 2009 L'Aquila earthquake (M_w 6.3). *Ital. J. Geosci.* **2012**, *131*, 309–329.
14. Lavecchia, G.; Ferrarini, F.; Brozzetti, F.; De Nardis, R.; Boncio, P.; Chiaraluce, L. From surface geology to aftershock analysis: Constraints on the geometry of the L'Aquila 2009 seismogenic fault system. *Ital. J. Geosci.* **2012**, *131*, 330–347.
15. Bigi, S.; Casero, P.; Chiarabba, C.; Di Bucci, D. Contrasting surface active faults and deep seismogenic sources unveiled by the 2009 L'Aquila earthquake sequence (Italy). *Terra Nov.* **2013**, *25*, 21–29. [[CrossRef](#)]
16. Bonini, L.; Di Bucci, D.; Toscani, G.; Seno, S.; Valensise, G. On the complexity of surface ruptures during normal faulting earthquakes: Excerpts from the 6 April 2009 L'Aquila (central Italy) earthquake (M_w 6.3). *Solid Earth* **2014**, *5*, 389–408. [[CrossRef](#)]
17. Castaldo, R.; de Nardis, R.; DeNovellis, V.; Ferrarini, F.; Lanari, R.; Lavecchia, G.; Pepe, S.; Solaro, G.; Tizzani, P. Coseismic Stress and Strain Field Changes Investigation Through 3-D Finite Element Modeling of DInSAR and GPS Measurements and Geological/Seismological Data: The L'Aquila (Italy) 2009 Earthquake Case Study. *J. Geophys. Res. Solid Earth* **2018**, *123*, 4193–4222. [[CrossRef](#)]
18. Guerrieri, L.; Baer, G.; Hamiel, Y.; Amit, R.; Blumetti, A.M.; Comerci, V.; Di Manna, P.; Michetti, A.M.; Salamon, A.; Mushkin, A.; et al. InSAR data as a field guide for mapping minor earthquake surface ruptures: Ground displacements along the Paganica Fault during the 6 April 2009 L'Aquila earthquake. *J. Geophys. Res. Solid Earth* **2010**, *115*, B12331. [[CrossRef](#)]

19. Chiarabba, C.; Amato, A.; Anselmi, M.; Baccheschi, P.; Bianchi, I.; Cattaneo, M.; Cecere, G.; Chiaraluce, L.; Ciaccio, M.G.; De Gori, P.; et al. The 2009 L'Aquila (central Italy) M_w 6.3 earthquake: Main shock and aftershocks. *Geophys. Res. Lett.* **2009**, *36*, L18308. [[CrossRef](#)]
20. Chiaraluce, L.; Valoroso, L.; Piccinini, D.; Di Stefano, R.; De Gori, P. The anatomy of the 2009 L'Aquila normal fault system (central Italy) imaged by high resolution foreshock and aftershock locations. *J. Geophys. Res. Solid Earth* **2011**, *116*, B12311. [[CrossRef](#)]
21. Calamita, F.; Satolli, S.; Scisciani, V.; Eserime, P.; Pace, P. Contrasting styles of fault reactivation in curved orogenic belts: Examples from the central Apennines (Italy). *Bull. Geol. Soc. Am.* **2011**, *123*, 1097–1111. [[CrossRef](#)]
22. Di Domenica, A.; Bonini, L.; Calamita, F.; Toscani, G.; Galuppo, C.; Seno, S. Analogue modeling of positive inversion tectonics along differently oriented pre-thrusting normal faults: An application to the Central-Northern Apennines of Italy. *Bull. Geol. Soc. Am.* **2014**, *126*, 943–955. [[CrossRef](#)]
23. Patacca, E.; Scandone, P. Post-Tortonian mountain building in the Apennines. The role of the passive sinking of a relic lithospheric slab. In *The Lithosphere in Italy*; Boriani, A., Bonafede, M., Piccardo, G.B., Vai, G.G., Eds.; Accademia Nazionale dei Lincei: Roma, Italy, 1989; pp. 157–176.
24. Barchi, M.; De Feyter, A.; Magnani, M.B.; Minelli, G.; Piali, G. The structural style of the Umbria-Marche fold and thrust belt. *Mem. Soc. Geol. It.* **1998**, *52*, 557–578.
25. Barba, S.; Basili, R. Analysis of seismological and geological observations for moderate-size earthquakes: The Colfiorito Fault System (Central Apennines, Italy). *Geophys. J. Int.* **2000**, *141*, 241–252. [[CrossRef](#)]
26. Toscani, G.; Seno, S.; Fantoni, R.; Rogledi, S. Geometry and timing of deformation inside a structural arc: The case of the western Emilian folds (Northern Apennine front, Italy). *Boll. della Soc. Geol. Ital.* **2006**, *125*, 59–65.
27. Cavinato, G.P.; Carusi, C.; Dall'asta, M.; Miccadei, E.; Piacentini, T. Sedimentary and tectonic evolution of Plio-Pleistocene alluvial and lacustrine deposits of Fucino Basin (central Italy). *Sediment. Geol.* **2002**, *148*, 29–59. [[CrossRef](#)]
28. Patacca, E.; Scandone, P.; Di Luzio, E.; Cavinato, G.P.; Parotto, M. Structural architecture of the central Apennines: Interpretation of the CROP 11 seismic profile from the Adriatic coast to the orographic divide. *Tectonics* **2008**, *27*. [[CrossRef](#)]
29. Tavarnelli, E.; Renda, P.; Pasqui, V.; Tramutoli, M. The effects of post-orogenic extension on different scales: An example from the Apennine-Maghrebide fold-and-thrust belt, SW Sicily. *Terra Nov.* **2003**, *15*, 1–7. [[CrossRef](#)]
30. Improta, L.; Villani, F.; Bruno, P.P.; Castiello, A.; De Rosa, D.; Varriale, F.; Punzo, M.; Brunori, C.A.; Civico, R.; Pierdominici, S.; et al. High-resolution controlled-source seismic tomography across the Middle Aterno basin in the epicentral area of the 2009, M_w 6.3, L'Aquila earthquake (central Apennines, Italy). *Ital. J. Geosci.* **2012**, *131*, 373–388.
31. D'Agostino, N.; Mantenuto, S.; D'Anastasio, E.; Giuliani, R.; Mattone, M.; Calcaterra, S.; Gambino, P.; Bonci, L. Evidence for localized active extension in the central Apennines (Italy) from global positioning system observations. *Geology* **2011**, *39*, 291–294. [[CrossRef](#)]
32. Anderson, H.; Jackson, J. Active tectonics of the Adriatic Region. *Geophys. J. R. Astron. Soc.* **1987**, *91*, 937–983. [[CrossRef](#)]
33. Roberts, G.P.; Michetti, A.M.; Cowie, P.; Morewood, N.C.; Papanikolaou, I. Fault slip-rate variations during crustal-scale strain localisation, central Italy. *Geophys. Res. Lett.* **2002**, *29*, 9-1–9-4. [[CrossRef](#)]
34. Vezzani, L.; Festa, A.; Ghisetti, F. Geological-structural map of the Central-Southern Apennines (Italy), 1:250,000 scale. Available online: <http://hdl.handle.net/2318/59925> (accessed on 24 August 2019).
35. Margheriti, L.; Chiaraluce, L.; Voisin, C.; Cultrera, G.; Govoni, A.; Moretti, M.; Bordoni, P.; Luzi, L.; Azzara, R.; Valoroso, L.; et al. Rapid response seismic networks in Europe: Lessons learnt from the L'Aquila earthquake emergency. *Ann. Geophys.* **2011**, *54*, 392–399.
36. Stucchi, M.; Camassi, R.; Rovida, A.; Locati, M.; Ercolani, E.; Meletti, C.; Migliavacca, P.; Bernardini, F.; Azzaro, R. DBMI04, il database delle osservazioni macrosismiche dei terremoti italiani utilizzate per la compilazione del catalogo parametrico CPTI04. *Quad. Geofis.* **2007**, *49*, 1–38.
37. Anzidei, M.; Boschi, E.; Cannelli, V.; Devoti, R.; Esposito, A.; Galvani, A.; Melini, D.; Pietrantonio, G.; Riguzzi, F.; Sepe, V.; et al. Coseismic deformation of the destructive April 6, 2009 L'Aquila earthquake (central Italy) from GPS data. *Geophys. Res. Lett.* **2009**, *36*, L17307. [[CrossRef](#)]

38. Cirella, A.; Piatanesi, A.; Cocco, M.; Tinti, E.; Scognamiglio, L.; Michelini, A.; Lomax, A.; Boschi, E. Rupture history of the 2009 L'Aquila (Italy) earthquake from non-linear joint inversion of strong motion and GPS data. *Geophys. Res. Lett.* **2009**, *36*, L19304. [[CrossRef](#)]
39. Cheloni, D.; D'Agostino, N.; D'Anastasio, E.; Avallone, A.; Mantenuto, S.; Giuliani, R.; Mattone, M.; Calcaterra, S.; Gambino, P.; Dominici, D.; et al. Coseismic and initial post-seismic slip of the 2009 Mw 6.3 L'Aquila earthquake, Italy, from GPS measurements. *Geophys. J. Int.* **2010**, *181*, 1539–1546.
40. Emergeo Working Group. *Rilievi Geologici di Terreno Effettuati Nell'area Epicentrale Della Sequenza Sismica Dell'aquilano del 6 Aprile 2009*; Istituto Nazionale di Geofisica e Vulcanologia: Rome, Italy, 2009; pp. 1–59.
41. Fujiwara, S.; Yarai, H.; Kobayashi, T.; Morishita, Y.; Nakano, T.; Miyahara, B.; Nakai, H.; Miura, Y.; Ueshiba, H.; Kakiage, Y.; et al. Small-displacement linear surface ruptures of the 2016 Kumamoto earthquake sequence detected by ALOS-2 SAR interferometry 4. Seismology 2016 Kumamoto earthquake sequence and its impact on earthquake science and hazard assessment Manabu Hashimoto, Martha Savage, Takuya Nishimura and Haruo Horikawa. *Earth Planets Sp.* **2016**, *68*, 160.
42. Bagnaia, R.; D'Epifanio, A.; Sylos Labini, S. Aquila and Subequan basins: an example of Quaternary evolution in central Apennines, Italy. *Quat. Nova*. **1992**, *II*, 187–209.
43. Vittori, E.; di Manna, P.; Blumetti, A.M.; Commerci, V.; Guerrieri, L.; Esposito, E.; Michetti, A.M.; Porfido, S.; Piccardi, L.; Roberts, G.P.; et al. Surface faulting of the 6 April 2009 mw 6.3 L'Aquila earthquake in central Italy. *Bull. Seismol. Soc. Am.* **2011**, *101*, 1507–1530. [[CrossRef](#)]
44. Albano, M.; Barba, S.; Saroli, M.; Moro, M.; Malvarosa, F.; Costantini, M.; Bignami, C.; Stramondo, S. Gravity-driven postseismic deformation following the Mw 6.3 2009 L'Aquila (Italy) earthquake. *Sci. Rep.* **2015**, *5*, 16558. [[CrossRef](#)]
45. Chiaraluce, L. Unravelling the complexity of Apenninic extensional fault systems: A review of the 2009 L'Aquila earthquake (Central Apennines, Italy). *J. Struct. Geol.* **2012**, *42*, 2–18. [[CrossRef](#)]
46. Falcucci, E.; Gori, S.; Peronace, E.; Fubelli, G.; Moro, M.; Saroli, M.; Giaccio, B.; Messina, P.; Naso, G.; Scardia, G.; et al. The Paganica Fault and Surface Coseismic Ruptures Caused by the 6 April 2009 Earthquake (L'Aquila, Central Italy). *Seismol. Res. Lett.* **2009**, *80*, 940–950. [[CrossRef](#)]
47. Thomas, A.L. Poly3D: A Three-dimensional, Polygonal Element, Displacement Discontinuity Boundary Element Computer Program with Applications to Fractures, Faults, and Cavities in the Earth's crust. Ph.D. Thesis, Stanford University, Stanford, CA, USA, June 1993.
48. Maerten, L.; Willemsse, E.J.M.; Pollard, D.D.; Rawnsley, K. Slip distributions on intersecting normal faults. *J. Struct. Geol.* **1999**, *21*, 259–272. [[CrossRef](#)]
49. Willemsse, E.J.M.; Pollard, D.D.; Aydin, A. Three-dimensional analyses of slip distributions on normal fault arrays with consequences for fault scaling. *J. Struct. Geol.* **1996**, *18*, 295–309. [[CrossRef](#)]
50. Crider, J.G.; Pollard, D.D. Fault linkage: Three-dimensional mechanical interaction between echelon normal faults. *J. Geophys. Res. Solid Earth* **1998**, *103*, 24373–24391. [[CrossRef](#)]
51. Madden, E.H.; Pollard, D.D. Integration of surface slip and aftershocks to constrain the 3D structure of faults involved in the M 7.3 landers earthquake, Southern California. *Bull. Seismol. Soc. Am.* **2012**, *102*, 321–342. [[CrossRef](#)]
52. Fattaruso, L.A.; Cooke, M.L.; Dorsey, R.J. Sensitivity of uplift patterns to dip of the San Andreas fault in the Coachella Valley, California. *Geosphere* **2014**, *10*, 1235–1246. [[CrossRef](#)]
53. Dorsett, J.H.; Madden, E.H.; Marshall, S.T.; Cooke, M.L. Mechanical Models Suggest Fault Linkage through the Imperial Valley, California, USA. *Bull. Seismol. Soc. Am.* **2019**. [[CrossRef](#)]
54. Yoffe, E.H. The angular dislocation. *Philos. Mag.* **1960**, *5*, 161–175. [[CrossRef](#)]
55. Comninou, M.; Dundurs, J. The angular dislocation in a half space. *J. Elast.* **1975**, *5*, 203–216. [[CrossRef](#)]
56. Brown, R.L. A dislocation approach to plate interaction. Ph.D. Thesis, Massachusetts Institute of Technology, Department of Earth and Planetary Sciences, Cambridge, MA, USA, August 1975.
57. Jeyakumaran, M. Modeling slip zones with triangular dislocation elements. *Bull. Seismol. Soc. America* **1992**, *82*, 2153–2169.
58. Maerten, F.; Resor, P.; Pollard, D.; Maerten, L. Inverting for slip on three-dimensional fault surfaces using angular dislocations. *Bull. Seismol. Soc. Am.* **2005**, *95*, 1654–1665. [[CrossRef](#)]
59. Cheng, L.W.; Lee, J.C.; Hu, J.C.; Chen, H.Y. Coseismic and postseismic slip distribution of the 2003 Mw = 6.5 Chengkung earthquake in eastern Taiwan: Elastic modeling from inversion of GPS data. *Tectonophysics* **2009**, *466*, 335–343. [[CrossRef](#)]

60. Bonini, L.; Basili, R.; Toscani, G.; Burrato, P.; Seno, S.; Valensise, G. The role of pre-existing discontinuities in the development of extensional faults: An analog modeling perspective. *J. Struct. Geol.* **2015**, *74*, 145–158. [[CrossRef](#)]
61. Pacor, F.; Spallarossa, D.; Oth, A.; Luzi, L.; Puglia, R.; Cantore, L.; Mercuri, A.; D'Amico, M.; Bindi, D. Spectral models for ground motion prediction in the L'Aquila region (central Italy): Evidence for stress-drop dependence on magnitude and depth. *Geophys. J. Int.* **2016**, *204*, 697–718. [[CrossRef](#)]
62. Yasar, E.; Erdogan, Y. Correlating sound velocity with the density, compressive strength and Young's modulus of carbonate rocks. *Int. J. Rock Mech. Min. Sci.* **2004**, *41*, 871–875. [[CrossRef](#)]
63. Allmann, B.P.; Shearer, P.M. Global variations of stress drop for moderate to large earthquakes. *J. Geophys. Res. Solid Earth* **2009**, *114*, B01310. [[CrossRef](#)]
64. Salazar-Mora, C.A.; Huismans, R.S.; Fossen, H.; Egydio-Silva, M. The Wilson Cycle and Effects of Tectonic Structural Inheritance on Rifted Passive Margin Formation. *Tectonics* **2018**, *37*, 3085–3101. [[CrossRef](#)]
65. Wilkinson, M.; McCaffrey, K.J.W.; Roberts, G.; Cowie, P.A.; Phillips, R.J.; Michetti, A.M.; Vittori, E.; Guerrieri, L.; Blumetti, A.M.; Bubeck, A.; et al. Partitioned postseismic deformation associated with the 2009 Mw 6.3 L'Aquila earthquake surface rupture measured using a terrestrial laser scanner. *Geophys. Res. Lett.* **2010**, *37*. [[CrossRef](#)]



© 2019 by the authors. Licensee MDPI, Basel, Switzerland. This article is an open access article distributed under the terms and conditions of the Creative Commons Attribution (CC BY) license (<http://creativecommons.org/licenses/by/4.0/>).